Received: 19 May 2021 | Revised: 8 October 2021 | Accepted: 14 October 2021

DOI: 10.1002/mp.15305

RESEARCH ARTICLE

MEDICAL PHYSICS

Block-matching-based registration to evaluate ultrasound visibility of percutaneous needles in liver-mimicking phantoms

Juan A. Sánchez-Margallo[1] | **Lisette Tas**[2] | **Adriaan Moelker**[3] | **John J. van den Dobbelsteen**[2] | **Francisco M. Sánchez-Margallo**[4] | **Thomas Langø**[5] | **Theo van Walsum**[6] | **Nick J. van de Berg**[3]

[1] Bioengineering and Health Technologies Unit, Jesús Usón Minimally Invasive Surgery Centre, Cáceres, Spain

[2] Department of Biomechanical Engineering, Delft University of Technology, Delft, The Netherlands

[3] Department of Radiology & Nuclear Medicine, Erasmus MC, University Medical Center Rotterdam, Rotterdam, The Netherlands

[4] Scientific Direction, Jesús Usón Minimally Invasive Surgery Centre, Cáceres, Spain

[5] SINTEF, Medical Technology, Trondheim, Norway

[6] Biomedical Imaging Group Rotterdam, Department of Radiology & Nuclear Medicine, Erasmus MC, University Medical Center Rotterdam, The Netherlands

Correspondence
Nick J. van de Berg, Department of Radiology & Nuclear Medicine, Erasmus MC, Doctor Molewaterplein 40, Rotterdam 3015 GD, The Netherlands.
Email: n.vandeberg@erasmusmc.nl

Funding information
ZonMw Program Innovative Medical Devices Initiative (IMDI) Life Sciences and Health, Grant/Award Number: 104003015; Junta de Extremadura (Spain); European Regional Development Fund (ERDF), Grant/Award Numbers: GR18199, TA18023; Norwegian National Advisory Unit for Ultrasound and Image-Guide Therapy at St. Olavs Hospital (Norway)

Abstract

Purpose: To present a novel methodical approach to compare visibility of percutaneous needles in ultrasound images.

Methods: A motor-driven rotation platform was used to gradually change the needle angle while capturing image data. Data analysis was automated using block-matching-based registration, with a tracking and refinement step. Every 25 frames, a Hough transform was used to improve needle alignments after large rotations. The method was demonstrated by comparing three commercial needles (14G radiofrequency ablation, RFA; 18G Trocar; 22G Chiba) and six prototype needles with different sizes, materials, and surface conditions (polished, sand-blasted, and kerfed), within polyvinyl alcohol phantom tissue and ex vivo bovine liver models. For each needle and angle, a contrast-to-noise ratio (CNR) was determined to quantify visibility. CNR values are presented as a function of needle type and insertion angle. In addition, the normalized area under the (CNR-angle) curve was used as a summary metric to compare needles.

Results: In phantom tissue, the first kerfed needle design had the largest normalized area of visibility and the polished 1 mm diameter stainless steel needle the smallest (0.704 ± 0.199 vs. 0.154 ± 0.027, $p < 0.01$). In the ex vivo model, the second kerfed needle design had the largest normalized area of visibility, and the sand-blasted stainless steel needle the smallest (0.470 ± 0.190 vs. 0.127 ± 0.047, $p < 0.001$). As expected, the analysis showed needle visibility peaks at orthogonal insertion angles. For acute or obtuse angles, needle visibility was similar or reduced. Overall, the variability in needle visibility was considerably higher in livers.

Conclusion: The best overall visibility was found with kerfed needles and the commercial RFA needle. The presented methodical approach to quantify ultrasound visibility allows comparisons of (echogenic) needles, as well as other technological innovations aiming to improve ultrasound visibility of percutaneous needles, such as coatings, material treatments, and beam steering approaches.

KEYWORDS
block-matching-based registration, bovine liver model, contrast-to-noise ratio, experimental methods, Hough transform, needle interventions, polyvinyl alcohol, ultrasound, visibility

1 | INTRODUCTION

1.1 | Clinical motivation

Needle identification in percutaneous ultrasound-guided procedures can be a challenging task, especially in situations where there is a suboptimal ultrasound (US) image quality. The quality may be reduced by numerous factors, such as the presence of isoechoic surrounding tissues, the presence of air or anatomical structures in the image that produce artifacts, reverberations, comet tails, or acoustic shadows. In addition, panel settings including gain, time gain compensation, and focus depth can be suboptimal for needle visualisation.[1] Other operator-related factors that may complicate needle identification include acute needle insertion angles, misalignment of the needle and imaging plane, loss of probe contact, or insufficient conductive gel. It is therefore not surprising that most interventional radiologists report that needles in interventional radiology procedures need to be improved in terms of visibility.[2]

During RFA in the liver, image guidance is critical for tumor targeting, process monitoring, and treatment response evaluation.[3] Inadequacies in image guidance can lead to incomplete tumor ablation.[4] Needle placement without proper visualization may result in unintentional vascular, neural, or visceral injury.[5] For US-guided RFA, tumor recurrence and residual tumor tissues are associated with incorrect needle placement and incomplete ablation, which are related to tumor size and location.[6] Many commercial and prototype solutions have been proposed to enhance visibility of needles in US imaging.[7,8] This includes needle designs and echogenic coatings,[9] but also enhancements in the imaging fields, for example, US beam steering.[10]

However, there is currently a lack of an objective and efficient approach for the evaluation of the visibility of percutaneous needles in ultrasound imaging, as well as of the efficacy of the existing methods for the improvement of visibility.[11] Percutaneous needle visibility analysis methods often contain manual steps, potentially introducing bias. The development of objective and automated evaluation methods would allow comparative studies to be carried out between different types of needles and techniques for visibility enhancement, and thus guide progress in this field.

1.2 | Related work

Metrics to objectively quantify needle visibility have been summarized in van de Berg et al.[11] Typically, they include a comparison of pixel intensity values sampled at well-defined image foreground (FG, needle) and adjacent background (BG, tissue) regions,[8,12] for example, a contrast-to-noise ratio (CNR).[13] After an image registration step, these visibility metrics may be retrieved using a local optimum search.

Image registration is the process of spatially aligning a *moving* image with a *target* image. Registration can be used in a multi-modality approach, by which pre-operative planning information (MRI, CT) becomes available during the intervention.[14,15] Alternatively, registration can be used in a single-modality approach, in which sequential images (real-time US) are matched and stabilized, for example, to track objects in motion or stabilize them in the image.

The US registration methods proposed in the scientific literature can be divided into feature-based and intensity-based approaches. Intensity-based approaches register entire images or sub-images with the aid of *similarity metrics* that compare intensity patterns. Here, sub-image center-points provide the corresponding feature points. In turn, feature-based methods register a set of distinct points, lines, or contours recognized in the image.

To register images during interventions in the liver, numerous methods have been proposed including speckle tracking,[16,17] optical flow-based methods,[18] landmark-intensity registration methods,[19] feature-based approaches using a Scale Invariant Feature Transform (SIFT),[20] and block-matching methods, in which feature-based and intensity-based properties are combined.[21] During block-matching, points are matched using intensity similarity, after which a global rigid-body transformation is computed that best superposes the corresponding points. A multitude of similarity metrics have been evaluated, including sum of squared differences (SSD), sum of absolute differences (SAD), and normalized cross-correlation (NCC).[22,23] Finally, an outlier rejection step has been proposed to improve block-matching results. In this step, aspects such as geometric consistency and appearance information can be evaluated.[22] In addition, to eliminate cumulative errors in the transform in case many sequential images are registered, block-matching can be implemented in a two-step approach consisting of a *tracking* and *refinement* step.[24]

1.3 | Contribution

Poor needle visibility is a persistent point of concern in interventional radiology, radiotherapy, and other clinical domains. A better understanding of causes of the suboptimal needle visibility is critical to improve future needle designs. This work has two major contributions. First, we bring together a methodical approach to evaluate visibility of percutaneous needles in ultrasound,[11] and a fast and robust block-matching based registration approach.[22] The registration fixes the needle position and orientation in the image and simplifies needle tracking and visibility computations. The end result is an

TABLE 1 Features of percutaneous needles included in the study

ID	Type	Diameter (mm)	Tip	Surface
Steel-p1	Steel (c)	1	Conical	P
Steel-p2	Steel (c)	2	Conical	P
Steel-sb	Steel (c)	2	Conical	SB
Steel-edm1	Steel (c)	2	Conical	EDM
Steel-edm2	Steel (c)	2	Conical	EDM
Niti-u	Nitinol (c)	2	Conical	U
Trocar-u	Trocar 18G	1.3	Diamond	U
Chiba-u	Chiba 22G	0.7	Bevel	U
RFA-u	RFA	2	Bevel	U

Abbreviations: c, custom-made; EDM, electric discharge machining; P, polishing; SB, sandblasting; U, unknown/untreated.

automated method for data collection and analysis of the visibility of percutaneous needles in ultrasound imaging. This is a translational step toward obtaining an in vivo metric that can be used as a sanity check to increase robustness or vigilance in automatic control and/or support tasks, as in the case of medical robotics,[25] when needle visibility is suboptimal.

Second, we use this method to compare the visibility of three commercially available needles (14G RFA, 18G Trocar, 22G Chiba) and six prototype needles for a large range of needle insertion angles. It extends our previous visibility study[11] with data from phantom tissue and ex vivo bovine liver models. The needles varied in diameters, materials, and surface treatments (treated by polishing, sandblasting, or electric discharge machining). After ultrasound image collection, data processing involved methods for filtering, line fitting, FG and BG sample selection, and image intensity analysis using CNR. A Hough-based feature recognition step was added to measure CNR values for large angular ranges. The area under the (CNR-angle) curve is used to compare the effectiveness of needle surface conditions on improving needle visibility in the ultrasound image.

2 | MATERIALS AND METHODS

2.1 | Percutaneous needles

Three factors that are considered important determinants for needle visibility are the needle material, the surface condition, and the needle diameter. Nine needles with different characteristics (Table 1) were included in this study (Figure 1). Three of them were commercially available: 18G needle (Trocar, Cook Medical, Bloomington, IN, USA), 22G needle (Chiba, Angiomed, Karlsruhe, Germany), and a 2 mm RFA needle (RITA StarBurst, AngioDynamics, Inc, Manchester, GA, USA). The other six needles were custom-made. Five of them had an outer diameter of 2 mm and one had an outer diameter of 1 mm. The surface of the custom-made needles was treated by polishing (P), sandblasting (SB), or electric discharge machining (EDM). Two needles contain kerfed EDM patterns resembling compliant joints in steerable needle designs.[26,27] Both kerf types were of equal size (width = 0.1 mm, depth = 0.5 mm), but the second had additional beveled edges (45° × 0.2 mm), which may increase the specular reflections for a specific insertion angle range. All custom-made needles were constructed from stainless steel (Steel), except for one, which was made from super-elastic nitinol (Nitinol). In the case of commercially available needles, the surface treatment was considered unknown (U).

2.2 | Rotation platform

Needles were inserted through a template and into a tissue specimen (Figure 1). The template was mounted on a rotation platform, actuated by a stepper motor (42BYGHM809, Wantai Motor, Jiangsu, China). The motor rotated the needle and specimen, while the probe was fixed, simulating gradual in-plane variations of needle insertion angles between 25–180°. The stepper motor was connected to a micro-stepping driver (Big Easy Driver, Sparkfun, Boulder, CO, USA) and operated at a constant angular speed of 0.1 rad/s (100 steps/s with 6 400 steps in 2π rad), using a microcontroller board (Arduino Uno R3, Arduino, Ivrea, Italy). Specimens were cylindrical in shape and the specimen–transducer contact was ensured with a linear micro-stage (PT1/M, Thorlabs, Newton, NJ, USA). To standardize beveled-tipped needle measurements, the bevel was always oriented toward the ultrasound transducer.

2.3 | Tissue specimens

The study was conducted in polyvinyl alcohol (PVA) phantoms, similar to the ones used in.[11] PVA is well-established as a soft tissue-mimicking material with similar acoustic properties to human tissue and is well suited for US imaging.[28,29] These specimens consisted of a 4 m% super-hydrolyzed PVA (Selvol PVOH 165, Sekisui Chemical Group, USA), 1 m% scattering agent (Silica gel 60, Merck Sharp & Dohme [MSD], Germany) solution in water. The solution was magnetically stirred and heated for 30 min at 93°C, before it was poured in the same cylindrical container. Once the specimens reached room temperature, they were placed in a freezer and subjected to two freeze–thaw cycles, according to the protocol described in de Jong et al.[28]

In addition, the experiment was conducted in an ex vivo model of bovine liver. To ensure the stability of the model and facilitate the acquisition of US images, the ex vivo specimen was embedded in a gelatine

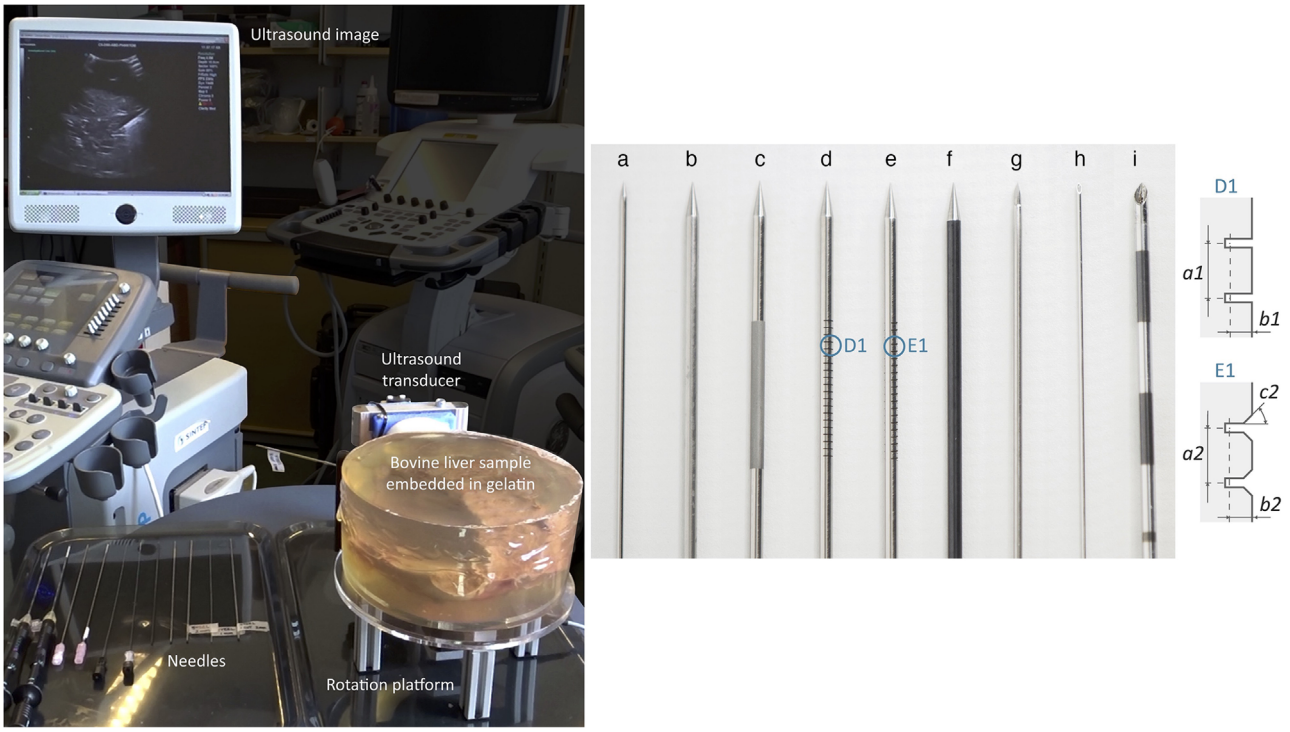

FIGURE 1 Experimental set-up with an ex vivo model of bovine liver and the set of percutaneous needles used. The overview of the set-up shows the liver sample, US transducer and US machine, as well as the needles used, including: (a) polished stainless steel (1 mm), (b) polished stainless steel (2 mm), (c) sand-blasted stainless steel (2 mm), (d) EDM stainless steel I (2 mm), (e) EDM stainless steel II (2 mm), (f) nitinol (2 mm), (g) trocar (18G), (h) chiba (22G), and (i) RFA (2 mm) needles. The kerfed needles are shown in a cross-sectional view, D1 and E1, where $a1 = a2 = 1$ mm, $b1 = b2 = 0.5$ mm, and $c2 = 45° \times 0.2$ mm

structure with a mass percent solution of 15 m% (Dr. Oetker Gelatine; Bielefeld, Germany). This resulted in cylindrical specimens with dimensions of 200 × 100 mm (diameter × height). Needles were inserted to a depth of 100 mm, so that their tips coincided approximately with the cylinder axis.

2.4 | Image acquisition and processing

For each needle type, ten runs were captured in bovine liver tissue and five runs in PVA. We used a curved-array transducer (C5-2/60, 2–5 MHz; Ultrasonix Medical Corporation, Richmond, Canada), connected to the US system (Ultrasonix MDP; Ultrasonix Medical Corporation). The US system was set to a frequency of 4 MHz, an imaging depth of 15 cm, and a depth of focus of 10 cm. The gain setting was set at 60% to limit clipping of image intensity values. CustusX image-guided therapy research platform was used to record the US images in each trial.[30] Images were imported and postprocessed in MeVisLab (MeVis Medical Solution AG, Bremen, Germany) and Python programs. Each image was aligned with respect to the first (reference) image for a robust and uniform needle visibility quantification.

2.5 | Ultrasound registration

Point-based rigid registration was performed in two steps, as presented in Banerjee et al.[24] In the *tracking step* (step-I), the most recent consecutive images, t_{n-1} and t_n, were aligned. The transformation matrices, T_n^{n-1}, were composed to obtain a total transformation estimate relative to the reference image, $\tilde{T}_n^{\text{ref}} = T_{n-1}^{\text{ref}} \circ T_n^{n-1}$. To minimize error accumulation, a *refinement step* (step-II) was used to match the transformed moving image with the reference image. This is equivalent to registering images t_{ref} and t_n in multiple small steps, instead of a single large step. Although the two-step approach is robust under conventional rotations,[24] the large rotations in our study result in changes in visible content, that is, other orthogonal faces of tissue structures light up. Therefore, to limit step-II outlier rejection, a new reference frame was taken every 25 frames. The resulting block-matching approach is visualized schematically in Figure 2.

2.6 | Block-matching

Registration point selection for block-matching was based on a regular grid with 10 mm spacing. A mask for

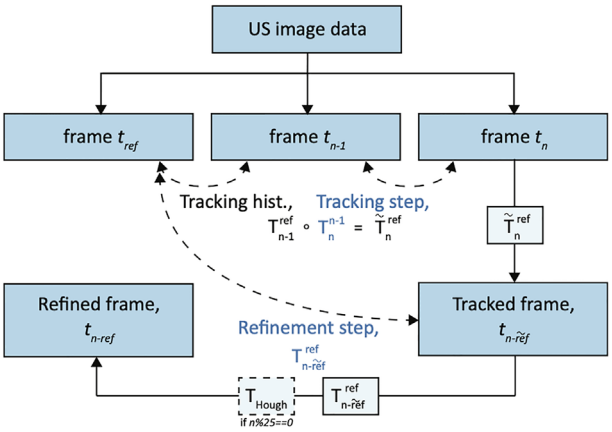

FIGURE 2 Two-step US image registration with block-matching. In the tracking step, consecutive images are rigidly aligned. The inverse of the tracking history and new tracking step combined is applied to frame t_n. This tracked frame is compared with the reference frame in a refinement step. For every 25th frame, a Hough correction is added. The refined frame $t_{n\text{-ref}}$ consists of frame t_n, transformed (T^{ref}_n) so that the needle is optimally aligned with the needle in reference frame t_{ref}

this grid was created using a binary image thresholding step ($T > 0$), followed by a morphology closing operation, with kernel sizes of $2n+1$ for the dilation ($n = 5$) and erosion ($n = 31$) steps. The mask and set of registration points are shown in Figure 3b.

For each registration point in the fixed image, a matching homologous point in the moving image was sought. This was done by selecting a block of size $B = (B_x,B_y) = (5,5)$ mm around each point and searching for a similar block within the search window $\Omega = (\Omega_x,\Omega_y) = (10,10)$ mm in the moving image. The group of corresponding points was subjected to an outlier rejection step that preserved distances between points (geometric constraint, $\sigma_G = 0.1$). NCC was used as a similarity metric for block-matching.[22] Although specimens were continuously rotating, inter-frame rotations were assumed sufficiently small so that block rotations were not required for matching.

Since we need to determine mean pixel intensity in image samples positioned on needles with diameters ranging between 0.7–2 mm, pixel-sized (0.271×0.271 mm) registration errors would already be large. Therefore, the selection of image FG and BG samples relied on a model-based fit, provided by the Hough line parameters orthogonal distance to origin (ρ) and line angle (θ).

2.7 | Hough line search

The Hough line search served three purposes. First of all, it was used to determine the initial needle angle, θ_0,

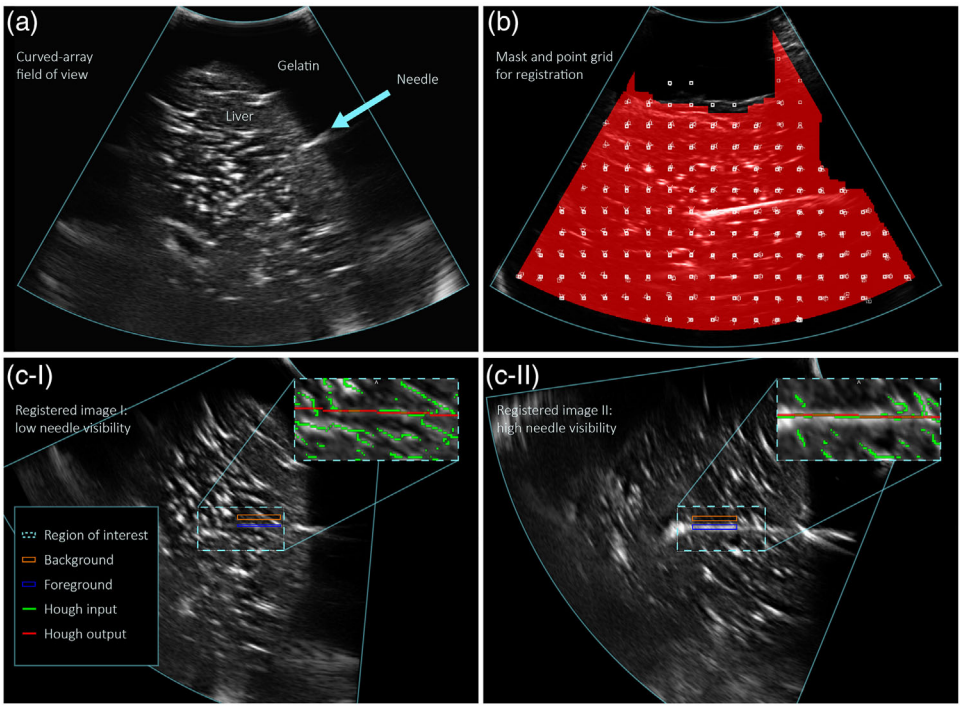

FIGURE 3 Image processing steps, showing: (a) an original US image, in this case with a needle with low visibility. The needle entry point (gelatine to liver) is still prominent. (b) The associative set of naive registration points, with vectors indicating the motion found between subsequent frames, and the mask used for point selection. (C) The registered image with the needle rotated horizontally, for the same image (c–i) and for a US image with a needle with higher visibility (c-II). Foreground and background image samples were collected from the region of interest (ROI), based on a Hough line search and CNR optimization. Input and output images for the Hough search are shown as green and red ROI overlays (right top corners), respectively

and orient the needle in the reference image horizontally. Second, the Hough line provided a local search area to evaluate needle visibility. Third, the line was used for a final correction (after the tracking and refinement registration steps) to keep needles aligned, since (1) the registration reference frame was renewed every 25 frames, and (2) the probe pushed against the rotating specimen, resulting in small non-rigid deformations, which cannot be corrected for using a rigid registration method.

The Hough-based correction was evaluated every 25th frame, upon reference image renewal. A correction consisted of a rotation and vertical translation to realign the needle, that is, the use of Hough line end-points for horizontal corrections was avoided as the needle is not equally visible along its full length. The correction was only performed when the CNR value of image t_{n-1} exceeded a threshold of 1 or 1.5, for runs in liver tissue and PVA, respectively. Values for this sanity check were determined empirically and aim to invalidate corrections when FG and BG samples were isoechoic. Since the values are low, corrections were accepted in most cases.

Hough analysis was performed within a 40 × 20 mm region of interest (ROI), with a fixed and central position in the image. The ROI was masked by an edge detection image of itself and Otsu's binarization was applied for intensity-based thresholding of detected edges, yielding a strongly reduced number of points for the Hough analysis (resolution: $\theta_{res} = 1°$, $\rho_{res} = 1$ pixel), shown in Figure 3c as green line segments. Edge detection consisted of sequentially applying a Sobel (y-direction, kernel size = 5 pixels) and Canny ($value_{min} = 127$, $value_{max} = 255$) filter. A search among Hough outputs was performed in which the minimum vote threshold was increased until ten or less needle candidates remained that complied to $|\theta - \theta_{est}| < 10°$ and $|\rho - \rho_{est}| < \frac{\Delta Y_{ROI}}{2}$, where $\theta_{est} = \frac{\pi}{2}$, $\rho_{est} = \rho_{n-1} \approx \frac{\Delta Y_{ROI}}{2}$ and $\Delta Y_{ROI} = 20$ mm. These conditions dictate that the lines are horizontal (with a maximum offset of $\Delta\theta = 10°$, in comparison 25 frames is ~7°), and pass through the ROI (location $\rho_{est} \approx \frac{\Delta Y_{ROI}}{2}$, with accepted departure $\Delta\rho = \frac{\Delta Y_{ROI}}{2}$). The line with the shortest vertical distance from the needle in image t_{n-1}, evaluated at $\frac{\Delta X_{ROI}}{2} = 20$ mm, was accepted. Finally, maximum needle visibility was evaluated in proximity to the moving median position of the needle in the last ten frames. These needle candidate reductions were needed to maintain a robust and automated approach even when visibility was poor or when other near-horizontal lines, for example, reverberations, appeared in the image.

2.8 | Needle visibility quantification

The CNR was used to evaluate the visibility of different needle shaft types in ultrasound images. CNR was defined as the absolute difference in image intensity between an FG, I_{FG}, and BG, I_{BG}, sample, divided by the standard deviation in BG intensity, σ_{BG}, as in[11]:

$$\mathrm{CNR}(n) = \frac{\left| I_{\bar{}FG}(n) - I_{\bar{}BG}(n) \right|}{\sigma_{BG}(n)}$$

The FG sample size was 20 × d mm, where d is the diameter of the specific needle. The BG samples all had a size of 20 × 2 mm. FG and BG samples were separated vertically by 2 mm (Figures 3c-I and 3c-II). A search was performed along the needle line to find the sampling location with the highest CNR. In this search, the y-coordinate was allowed to deviate ±1 mm from the line (resolution 0.5 mm in x and y). For each image, the registration angle, θ_r, and CNR value were stored in a text file. Needle insertion angles were determined by combining initial and registration angles, that is, $\theta = \theta_0 + \theta_r$.

The dataset was sorted to ensure a monotonic increase of θ, resampled (interpolation, θ_0:0.01:π) and filtered (moving average, window = 5 data points) to compute means and SDs along equal evaluation windows. Polar plots showing the mean and SD of needle visibility (CNR) versus insertion angle (θ) were created for each needle type. For each study model (PVA and liver tissue), the area of visibility covered by each needle was calculated. This area is defined as the accumulation of CNR values over the needle insertion angle range ($\sum$CNR). The CNR values were normalized with respect to the maximum value of each model. The results obtained for each needle were presented and compared with Wilcoxon signed-rank tests in R version 4.00 (R Foundation for Statistical Computing, Vienna, Austria). In addition, differences are indicated by means of notched box plots. Every notched box has a line marking the lower, median and upper quartile values, and whiskers represent the extent of the remaining data, with dots showing the outliers. The boxes whose notches do not overlap are significantly different ($p < 0.05$).

3 | RESULTS

The results show an increase in CNR values in the ex vivo model compared to the PVA model (Figures 4 and 5). However, this increase is strongly centered at the orthogonal needle angle, whereas CNR values in the bulk of the angular range appear to be either equal or lower in the ex vivo model, that is, the peak is a lot more pronounced. The liver model data show higher values and higher variability in visibility, compared to the PVA model. Changes in diameter (steel 1 mm vs. 2 mm) or material type (steel 2 mm vs. Niti 2 mm) did not present

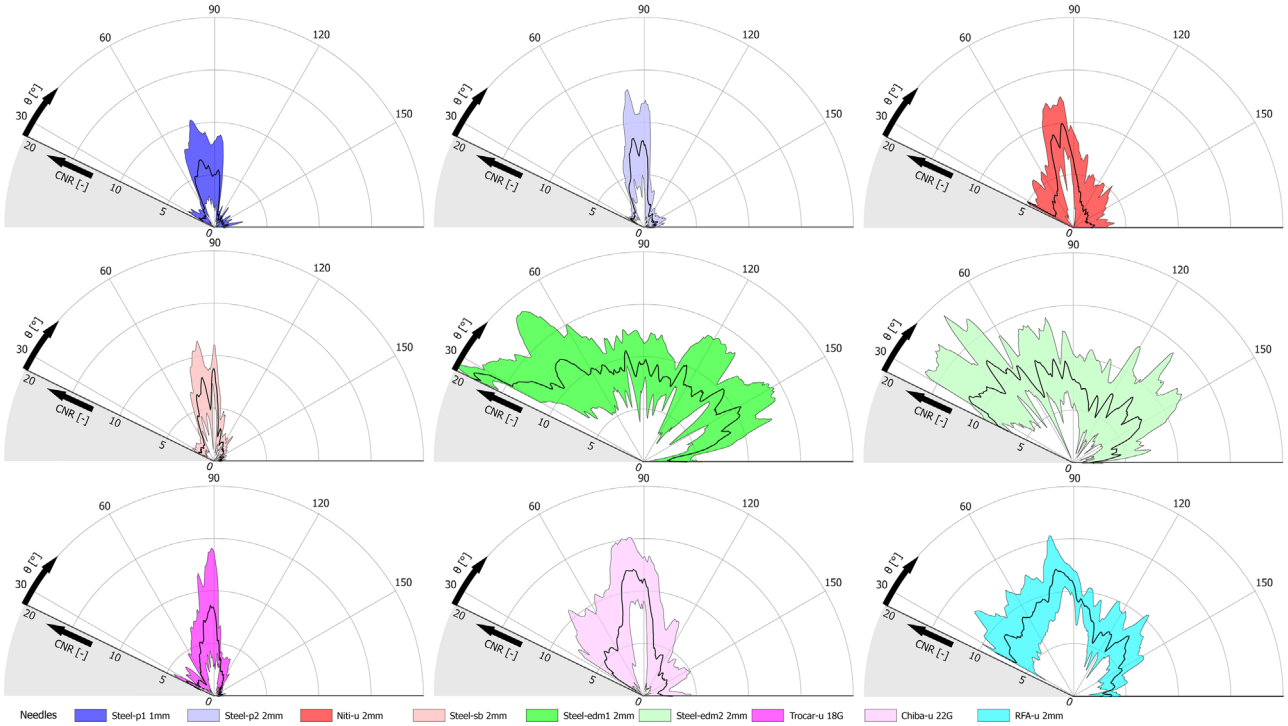

FIGURE 4 Needle visibility in PVA as a function of the insertion angle, showing means as black lines and mean ± standard deviations as colored bands, based on five measurements per condition. Abbreviations: Chiba-u 22G, Chiba needle; CNR, contrast-to-noise ratio; Niti-u 2 mm, nitinol needle; RFA-u 2 mm: RFA needle; Steel-edm1 2 mm, EDM stainless steel I needle; Steel-edm2 2 mm, EDM stainless steel II needle; Steel-p1 1 mm, polished stainless steel needle; Steel-p2 2 mm, polished stainless steel needle; Steel-sb 2 mm, sand-blasted stainless steel needle; Trocar-u 18G, trocar needle

clear effects on visibility. Results show that the steel-EDM (with kerfs) and RFA needles are visible over a wider range of insertion angles for both ex vivo and PVA models. The kerfed needles provided the best visibility results.

In the PVA model, the EDM1 needle had the highest area of visibility covered and the 1 mm Steel-p1 the smallest (0.704 ± 0.199 vs. 0.154 ± 0.027, $p < 0.01$). The two EDM needles (EDM1: 0.704 ± 0.199, EDM2: 0.583 ± 0.184) and the RFA needle (0.545 ± 0.065) obtained similar results (Figure 6). The three needles showed a statistically significant increase in the area of visibility with respect to the rest ($p < 0.05$), except for the Chiba-u needle (0.352 ± 0.202).

Regarding the overall visibility in liver tissue, the EDM2 needle (0.470 ± 0.190) performed better than most other needles (significant difference for 6 out of 8 designs), with the Steel-sb 2 mm needle covering the smallest area of visibility (0.470 ± 0.190 vs. 0.127 ± 0.047, $p < 0.001$). This was followed by the RFA needle (5/8) and EDM1 needle (3/8) (RFA: 0.380 ± 0.240, EDM1: 0.324 ± 0.176) (Figure 7). Although the EDM2 needle has the best performance in the liver tissue environment, in the PVA model the difference with the EDM1 and RFA appears to be less pronounced.

4 | DISCUSSION

In this work, the relation between CNR and the insertion angle was studied in PVA and ex vivo bovine liver models, for a series of prototype and commercially available needles. Collection of data was automated by a motor-driven rotation platform that gradually varied the angle between the needle and the US probe (the insertion angle). In addition, the data analysis was automated by a two-step block-matching based registration that aligned needles in sequential frames and enabled subsequent quantification of needle visibility. Other objective methods for the analysis of visibility of percutaneous needles based on image intensity have been presented.[8,12,13,31] However, these analyses contained manual steps, possibly introducing bias. In addition, they typically use a selection of needle insertion angles, whereas we present the full range of angles.

Needle visibility is strongly dependent on the insertion angle, where the highest values are seen at orthogonal needle-probe angles (Figures 4 and 5). Other studies also reported an increase in visibility of the needle near the 90° angle.[13,32] This effect is caused by specular reflections of US waves at the needle surface, returning to the probe for orthogonal angles, but not for acute angles. Of more interest is the *width* of the

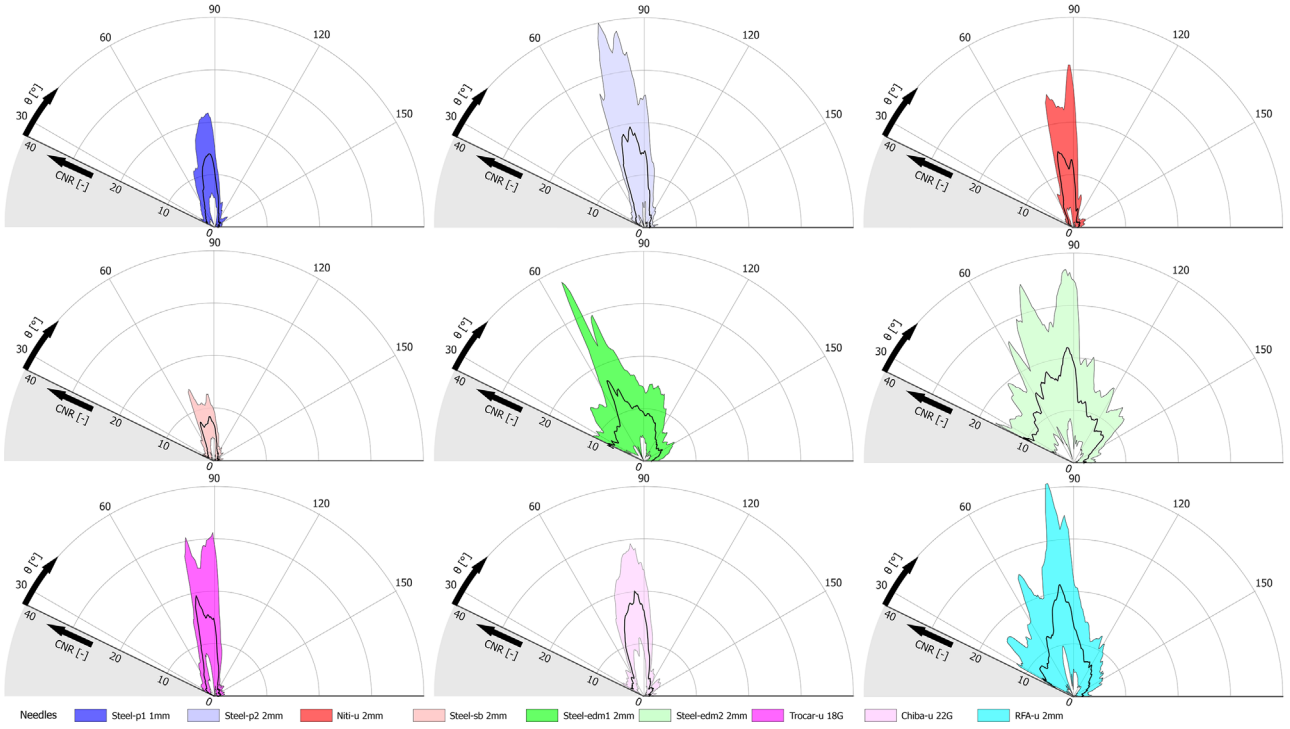

FIGURE 5 Needle visibility in liver tissue as a function of the insertion angle, showing means as black lines and mean ± standard deviations as colored bands, based on 10 measurements per condition. Abbreviations: Chiba-u 22G, Chiba needle; CNR , contrast-to-noise ratio; Niti-u 2 mm, nitinol needle; RFA-u 2 mm, RFA needle; Steel-edm1 2 mm, EDM stainless steel I needle; Steel-edm2 2 mm, EDM stainless steel II needle; Steel-p1 1 mm, polished stainless steel needle; Steel-p2 2 mm, polished stainless steel needle; Steel-sb 2 mm, sand-blasted stainless steel needle; Trocar-u 18G, trocar needle

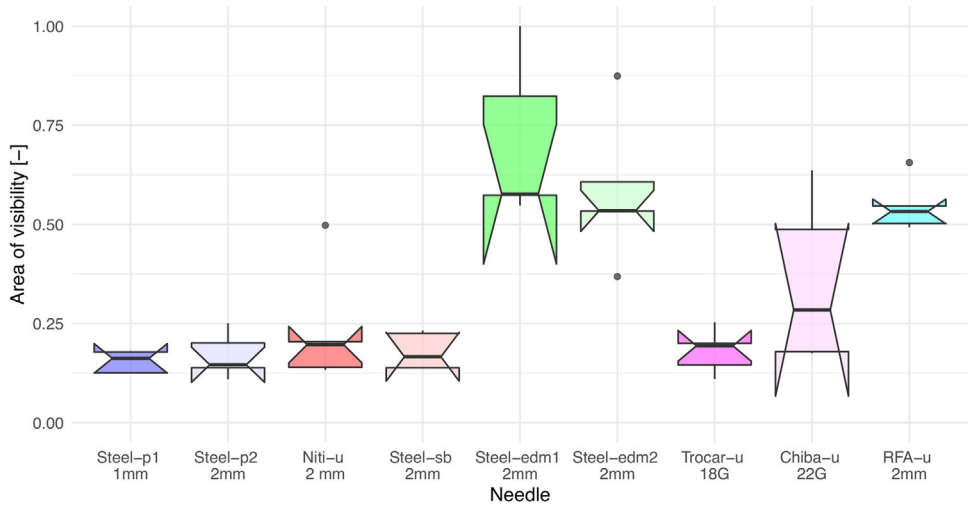

FIGURE 6 Comparison between the areas defined by the CNR value according to the insertion angle of the needle in the PVA model. The values of the area of visibility have been normalized to their maximum value (1,975.076 CNR*degree). Abbreviations: Chiba-u 22G, Chiba needle; Niti-u 2 mm, nitinol needle; RFA-u 2 mm, RFA needle; Steel-edm1 2 mm, EDM stainless steel I needle; Steel-edm2 2 mm, EDM stainless steel II needle; Steel-p1 1 mm, polished stainless steel needle; Steel-p2 2 mm, polished stainless steel needle; Steel-sb 2 mm, sand-blasted stainless steel needle; Trocar-u 18G, trocar needle

specular reflection peak or the *surface area* under the curve. A comparison of surface areas showed that material treatments, such as the addition of kerfs by EDM, can remarkably improve overall needle visibility (Figures 6 and 7). It seems that alterations to the needle surface help enhance visibility under US imaging. Other studies also showed that the use of percutaneous needles with mechanical modifications on the surface improved

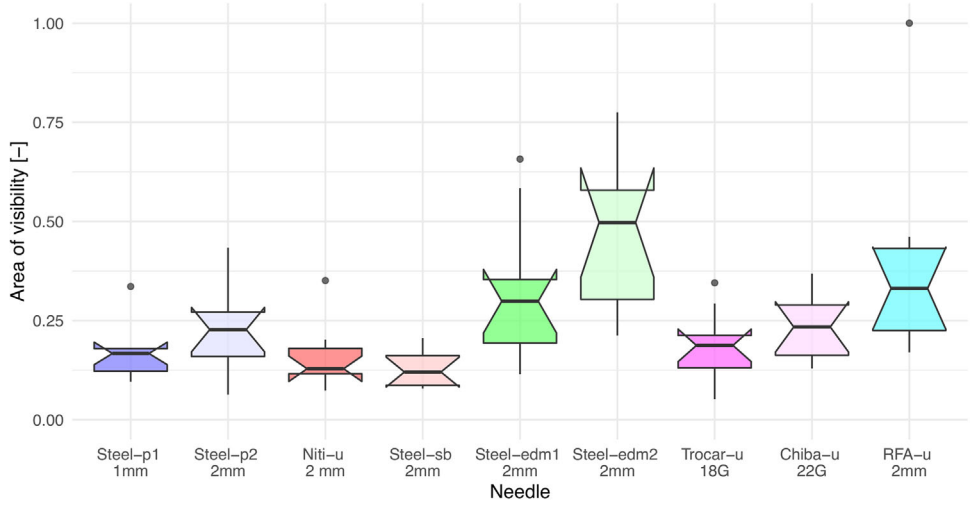

FIGURE 7 Comparison between the areas defined by the CNR value according to the insertion angle of the needle in liver tissue. The values of the area of visibility have been normalized to their maximum value (3,129.562 CNR*degree). Abbreviations: Chiba-u 22G, Chiba needle; Niti-u 2 mm, nitinol needle; RFA-u 2 mm, RFA needle; Steel-edm1 2 mm, EDM stainless steel I needle; Steel-edm2 2 mm, EDM stainless steel II needle; Steel-p1 1 mm, polished stainless steel needle; Steel-p2 2 mm, polished stainless steel needle; Steel-sb 2 mm, sand-blasted stainless steel needle; Trocar-u 18G, trocar needle

their visualization.[8,12] In addition, we have found that the included RFA needle has a relatively high visibility (Figures 6 and 7). This needle is hollow and contains pre-curved tines that can protrude to increase ablation zones (they were retracted in this study). The metal–air density transitions within the needle may have increased reflections and improved visibility for a larger range of angles. Another material-related factor that could affect the visibility of RFA needles is their electrically insulating coating. Arif et al. also obtained better visibility results for the ablation needles, including RFA, in a comparative study with commercial percutaneous needles.[13] However, they analyzed the visibility of the needle tips under 3D ultrasound imaging.

When comparing results in PVA and liver tissue, the 90° angle peak was less prominent in the PVA model (Figure 4) than in the ex vivo model (Figure 5), giving the appearance that the overall visibility was higher. However, it should be noted that different radial plot axes were used, as variability in data in liver tissue was much higher than in PVA. In some cases, BG samples in the liver could be near-black (i.e., $\sigma_{BG} \approx 0$), causing a rapid increase in CNR. In other cases, BG and FG samples were isoechoic. In PVA, the BG sample was overall more consistent in intensity. This was expected as PVA is a relatively homogeneous material, whereas liver specimens contain different tissues and transitions between structures, including ligaments and vasculature, resulting in local variations in US image intensity.

The CNR profile shapes and magnitudes in PVA resemble those in our previous needle shaft visibility quantification, in which a different US machine, image capturing method, and data analysis were used.[11] In our former work, we initialized the analysis by interpolating needle positions and angles based on manual needle delineations in two frames, at the start and end of captured videos. Our current work required only an insertion angle estimate for the initiating Hough transform, as needle visibility was not always high for the acute starting angles. The registration uses a naive and evenly distributed set of points in the US image and does not specifically focus on needle stabilization. Therefore, the Hough analysis was repeated every 25 frames to improve needle alignment between frames under minor non-rigid deformations. In accordance with the results presented in the previous study, the kerfed needles showed the best visibility results in the ultrasound images (Figures 6 and 7).

The registration correction process is based on the Hough transform, which is a robust algorithm for detecting linear features in images, making it a widely used technique for detecting needles in US images. This feature extraction technique has been used in other studies to address the difficulties of needle visualization in US-guided procedures, mainly for needle detection,[33] including curved needles.[34] Similarly, it has been used to develop automated methods for steering the ultrasound beam and keeping it perpendicular to the needle during the procedure to enhance its visualization.[35] The feasibility of the application of this algorithm has also been tested in the segmentation of needles in 3D US images.[36] In addition to needle identification, a method for real-time tracking of percutaneous needles in US images has been developed by combining Hough transform and optical flow techniques.[37]

The registration of US images based on a rigid registration method has some limitations. With the US probe pushing against our rotating specimens, minor non-rigid deformations were observed. Non-rigid registration methods could be implemented to address deformations of the liver, also during real interventions. In addition, our analysis did not require a needle tracking step, which would be needed to evaluate visibility during needle insertion. Real-time tracking of needles and quantifying of visibility could assist uncertainty-based path planning, for example, to avoid taking resolute control decisions based on poor image conditions. In our current work, we demonstrated this potential use of CNR as a sanity check by accepting the Hough transform correction only when the needle visibility in image t_{n-1} exceeded a predefined threshold.

5 | CONCLUSIONS

This article presents an automated and objective approach to evaluate visibility of percutaneous needles in ultrasound images, using block-matching-based registration. In addition, the approach is evaluated in both phantom tissue and ex vivo bovine liver models, by comparing the effect of diameter, material type, and surface treatment on needle visibility. Visibility data (CNR values) were collection for a full range of needle insertion angles. The analysis presented a higher visibility performance for the kerfed needles. In particular, needle visibility was high near the orthogonal insertion angles. The approach can be used to compare technological innovations, such as echogenic coatings, material treatments, and beam steering methods. It may also be developed into a quality check for automated planning or robotized execution of needle interventions.

ACKNOWLEDGMENTS

This work was supported by the ZonMw Program Innovative Medical Devices Initiative (IMDI) Life Sciences and Health (No. 104003015), the Junta de Extremadura (Spain), the European Regional Development Fund (ERDF) (GR18199, TA18023), and the Norwegian National Advisory Unit for Ultrasound and Image-Guide Therapy at St. Olavs Hospital (Norway). The authors would like to thank Arjan van Dijke for his contribution in the development of the rotation platform.

CONFLICT OF INTEREST

The authors declare that there is no conflict of interest that could be perceived as prejudicing the impartiality of the research reported.

DATA AVAILABILITY STATEMENT

The data that support the findings of this study are available from the corresponding author upon reasonable request.

REFERENCES

1. Reusz G, Sarkany P, Gal J, Csomos A. Needle-related ultrasound artifacts and their importance in anaesthetic practice. *Brit J Anaesth*. 2014;112:794-802.
2. de Jong TL, van de Berg NJ, Tas L, Moelker A, Dankelman J, van den Dobbelsteen JJ. Needle placement errors: do we need steerable needles in interventional radiology? *Med Devices Evid Res*. 2018;11:259-265.
3. Wiggermann P, Zuber-Jerger I, Zausig Y, et al. Contrast-enhanced ultrasound improves real-time imaging of ablation region during radiofrequency ablation: preliminary results. *Clin Hemorheol Microcirc*. 2011;49:43-54.
4. Chin KA, Perlas A, Chan VWS, Brull R. Needle visualization in ultrasound-guided regional anesthesia: challenges and solutions. *Reg Anesth Pain Med*. 2008;33:532-544.
5. Künzli BM, Abitabile P, Maurer CA. Radiofrequency ablation of liver tumors: actual limitations and potential solutions in the future. *World J Hepatol*. 2011;3:8-14.
6. Hori T, Nagata K, Hasuike S, et al. Risk factors for the local recurrence of hepatocellular carcinoma after a single session of percutaneous radiofrequency ablation. *J Gastroenterol*. 2003;38:977-981.
7. Miura M, Takeyama K, Suzuki T. Visibility of ultrasound-guided echogenic needle and its potential in clinical delivery of regional anesthesia. *Tokai J Exp Clin Med*. 2014;39:80-86.
8. Bigeleisen PE, Hess A, Zhu R, Krediet A. Modeling, production, and testing of an echogenic needle for ultrasound guided nerve blocks. *J Ultrasound Med*. 2016;35:1319-1323.
9. de Korte CL, Weijers G, Vriezema DM, Keereweer AR, Thijssen JM, Hansen HHG. Quantitative analysis of coated needles for ultrasound guided intervention. *Proc IEEE Int Ultrason Symp*. 2012:1571-1574.
10. Hatt CR, Ng G, Parthasarathy V. Enhanced needle localization in ultrasound using beam steering and learning-based segmentation. *Comput Med Imaging Graph*. 2015;41:46-54.
11. van de Berg NJ, Sanchez-Margallo JA, van Dijke AP, Lango T, van den Dobbelsteen JJ. A methodical quantification of needle visibility and echogenicity in ultrasound images. *Ultrasound Med Biol*. 2019;45:998-1009.
12. Nakagawa K, Kamiya T, Arakawa K, Akiyama S, Sakai K. Objective and subjective comparison of the visibility of three echogenic needles and a nonechogenic needle on older ultrasound devices. *Acta Anaesthesiol Taiwan*. 2015;53:1-6.
13. Arif M, Moelker A, van Walsum T. Needle tip visibility in 3D ultrasound images. *Cardiovasc Intervent Radiol*. 2018;41:145-152.
14. Blackall JM, Penney GP, King AP, Hawkes DJ. Alignment of sparse freehand 3D ultrasound with preoperative images of the liver using models of respiratory motion and deformation. *IEEE Trans Med Imaging*. 2005;24:1405-1416.
15. Wein WG, Brunke S, Khamene A, Callstrom MR, Navab N. Automatic CT–ultrasound registration for diagnostic imaging and image-guided intervention. *Med Image Anal*. 2008;12:577-585.
16. Bell MAL, Byram BC, Harris EJ, Evans PM, Bamber JC. In vivo liver tracking with a high volume rate 4D ultrasound scanner and a 2D matrix array probe. *Phys Med Biol*. 2012;57:1359-1374.
17. Harris EJ, Miller NR, Bamber JC, Symonds-Tayler JRN, Evans PM. Speckle tracking in a phantom and feature-based tracking in liver in the presence of respiratory motion using 4D ultrasound. *Phys Med Biol*. 2010;55:3363-3380.
18. Williamson T, Cheung W, Roberts SK, Chauhan S. Ultrasound-based liver tracking utilizing a hybrid template/optical flow approach. *Int J Comput Assist Radiol*. 2018;13:1605-1615.
19. Lange T, Papenberg N, Heldmann S, et al. 3D ultrasound-CT registration of the liver using combined landmark-intensity information. *Int J Comput Assist Radiol*. 2009;4:79-88.
20. Schneider RJ, Perrin DP, Vasilyev NV, Marx GR, del Nido PJ, Howe RD. Real-time image-based rigid registration of three-dimensional ultrasound. *Med Image Anal*. 2012;16:402-414.

21. Commowick O, Wiest-Daessle N, Prima S, Block-matching strategies for rigid registration of multimodal medical images. *2012 9th IEEE International Symposium on Biomedical Imaging (ISBI)*. IEEE; 2012:700-703.
22. Banerjee J, Klink C, Peters ED, Niessen WJ, Moelker A, van Walsum T. Fast and robust 3D ultrasound registration: block and game theoretic matching. *Med Image Anal*. 2015;20:173-183.
23. Markelj P, Tomazvic D, Likar B, Pernus F. A review of 3D/2D registration methods for image-guided interventions. *Med Image Anal*. 2012;16:642-661.
24. Banerjee J, Klink C, Niessen WJ, Moelker A, van Walsum T. 4D ultrasound tracking of liver and its verification for TIPS guidance. *IEEE Trans Med Imaging*. 2016;35:52-62.
25. Chevrie J, Shahriari N, Babel M, Krupa A, Misra S. Flexible needle steering in moving biological tissue with motion compensation using ultrasound and force feedback. *IEEE Robot Autom Lett*. 2018;3:2338-2345.
26. Henken KR, Seevinck PR, Dankelman J, van den Dobbelsteen JJ. Manually controlled steerable needle for MRI-guided percutaneous interventions. *Med Biol Eng Comput*. 2017;55:235-244.
27. van de Berg NJ, Meeuwsen FC, Doukas M, Kronreif G, Moelker A, van den Dobbelsteen JJ. Steerable needles for radio-frequency ablation in cirrhotic livers. *Sci Rep*. 2021;11(1):309.
28. de Jong TL, Pluymen LH, van Gerwen DJ, Kleinrensink GJ, Dankelman J, van den Dobbelsteen JJ. PVA matches human liver in needle–tissue interaction. *J Mech Behav Biomed*. 2017;69:223-228.
29. Surry KJM, Austin HJB, Fenster A, Peters TM. Poly(vinyl alcohol) cryogel phantoms for use in ultrasound and MR imaging. *Phys Med Biol*. 2004;49:5529-5546.
30. Askeland C, Solberg OV, Bakeng JBL, et al. CustusX: an open-source research platform for image-guided therapy. *Int J Comput Assist Radiol*. 2016;11:505-519.
31. Schafhalter-Zoppoth I, McCulloch CE, Gray AT. Ultrasound visibility of needles used for regional nerve block: an in vitro study. *Reg Anesth Pain Med*. 2004;29:480-488.
32. Francis KJ, Manohar S. Photoacoustic imaging in percutaneous radiofrequency ablation: device guidance and ablation visualization. *Phys Med Biol*. 2019;64:184001.
33. Chan C, Lam F, Rohling R. A needle tracking device for ultrasound-guided percutaneous procedures. *Ultrasound Med Biol*. 2005;31:1469-1483.
34. Okazawa SH, Ebrahimi R, Chuang J, Rohling RN, Salcudean SE. Methods for segmenting curved needles in ultrasound images. *Med Image Anal*. 2006;10:330-342.
35. Cheung S, Rohling R. Enhancement of needle visibility in ultrasound-guided percutaneous procedures. *Ultrasound Med Biol*. 2004;30:617-624.
36. Zhou H, Qiu W, Ding MY, Zhang SG. Automatic needle segmentation in 3D ultrasound images using 3D improved Hough transform. *Proc SPIE 6789, MIPPR 2007: Medical Imaging, Parallel Processing of Images, and Optimization Techniques*. 2008.
37. Ayvali E, Desai JP. Optical flow-based tracking of needles and needle-tip localization using circular Hough transform in ultrasound images. *Ann Biomed Eng*. 2015;43:1828-1840.

How to cite this article: Sánchez-Margallo JA, Tas L, Moelker A, et al. Block-matching-based registration to evaluate ultrasound visibility of percutaneous needles in liver-mimicking phantoms. *Med Phys*. 2021;48:7602–7612. https://doi.org/10.1002/mp.15305